Journal of Inorganic and Organometallic Polymers and Materials (2024) 34:3076–3088
https://doi.org/10.1007/s10904-024-03165-6

RESEARCH

A Tris(terpyridine) Ligand-based Metal Coordination Nanosheet as Electrode Material with Good Supercapacitor Performance

Qian Liu[1] · Zhiwei Xu[1] · Zengqi Guo[1] · Su Guo[1] · Mengru Huang[1] · Wai-Yeung Wong[2]

Received: 8 May 2024 / Accepted: 24 May 2024 / Published online: 4 July 2024

Abstract

In this work, through a facile liquid–liquid (L–L) interfacial-assisted synthesis at room temperature, a new two-dimensional (2D) metal coordination nanosheet Co-TPY-LB has been synthesized by the coordination between Co^{2+} ion and 1,3,5-tris(4′-tripyridinylphenyl)benzene (Tris-tpy). The flat and smooth sheet structure with a thickness of 83.3 nm and a hexagonal structure with a lattice spacing of about 0.206 nm for the as-fabricated nanosheet Co-TPY-LB has been identified by AFM and HRTEM respectively, providing a large number of redox sites and ion diffusion channels. The fabricated Co-TPY-LB have been used as electrodes and exhibit the highest capacity of 2741.5 F g^{-1} at the current density of 1 A g^{-1}, an excellent cycling stability with 97.6% capacity retention after 1000 cycles at the current density of 10 A g^{-1}. Meanwhile, the assembled asymmetric supercapacitor with Co-TPY-LB as the positive electrode shows a high energy density 73.6 Wh kg^{-1} at a power density of 4800 W kg^{-1} as well as an excellent cycle stability of 92.9% capacity retention after 5000 cycles. Our work provides a controllable synthesis for the construction of 2D metal coordination nanosheet to overcome some defects of 2D nanosheet by traditional synthesis, leading such bottom-up nanosheet to a promising application in energy storage.

✉ Qian Liu
lqcz_2008@ahpu.edu.cn

✉ Wai-Yeung Wong
wai-yeung.wong@polyu.edu.hk

[1] Anhui Province Key Laboratory of Functional Coordinated Complexes for Materials Chemistry and Application, School of Chemical and Environmental Engineering, Anhui Polytechnic University, Wuhu 241000, People's Republic of China

[2] Department of Applied Biology and Chemical Technology and Research Institute for Smart Energy, The Hong Kong Polytechnic University, Hung Hom, Kowloon, Hong Kong, People's Republic of China

Graphical Abstract

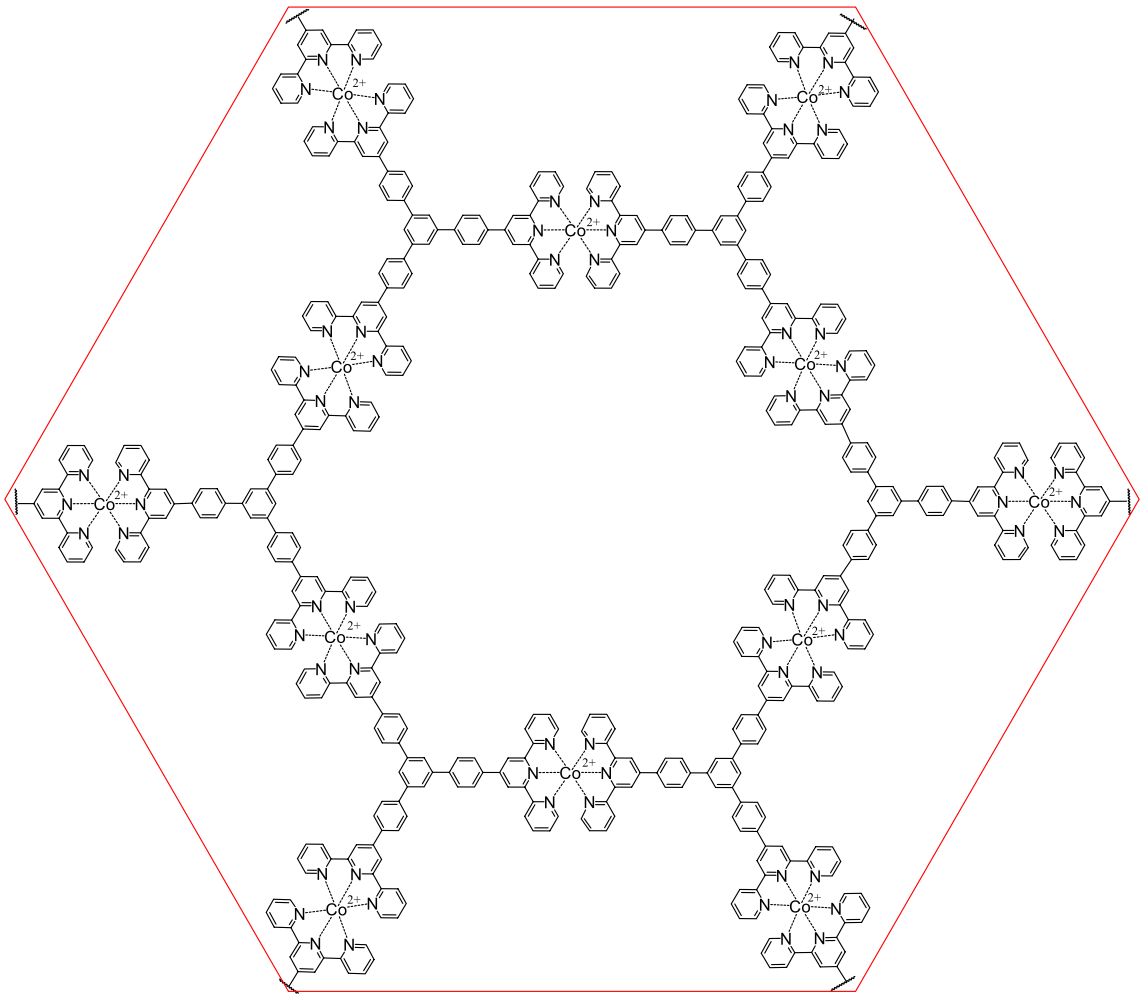

Keywords Controllable synthesis · Metal coordination nanosheet · Electrochemistry · Electrode materials · Supercapacitor

1 Introduction

With the rapid development of electronic devices such as wearable devices, mobile phones, laptops, and the emergence of many issues such as rising oil prices and air pollution, there is a great demand for the introduction of flexible, lightweight, high-performance and sustainable energy storage devices, such as batteries [1, 2] solar cells [3, 4] and supercapacitors, in which supercapacitors have attracted much more attention, due to their light weight, high energy density, fast charge–discharge kinetics, excellent reversibility, and excellent cycling stability [5–8]. Although supercapacitors exhibit high power density, their relatively low energy density and poor energy output hinder their further application [9]. In order to improve the energy density of supercapacitors without sacrificing their high power density, the development of electrode materials is considered a key factor in determining the electrochemical storage capacity [10]. Metal–organic frameworks (MOFs) containing metal centers and organic linkers have emerged and attracted increasing attention in the field of electrochemical energy storage in the past two decades [11]. Particularly, two-dimensional (2D) MOFs with graphene-like structures are considered as very promising electrodes for supercapacitors, because of their good conductivity, high surface area and numerous active sites. The most common traditional synthesis method for 2D MOF nanosheet is the hydrothermal method. For example, Han and co-workers synthesized a 2D conductive MOF (Ni-CAT) as a flexible free-standing membrane by combining electrospinning technology with hydrothermal method, which was used as electrode and showed high specific capacitance of 502.95 F g^{-1} at a current

density of 0.5 A g^{-1} and an improved cycling stability of 73% capacitance retention over 5000 cycles as an electrode material for supercapacitors. The asymmetric supercapacitor based on CNF@Ni-CAT and active carbon (AC) shows an energy density of 18.67 Wh kg^{-1} at a power density of 297.12 W kg^{-1} and maintains 106.19% of the original specific capacitance after 5000 cycles [12]. By hydrothermal method, Wang and co-workers obtained the Ni-MOF/CNTs, which shows an excellent electrochemical performance to achieve a high specific capacitance of 1765 F g^{-1} at a current density of 0.5 A g^{-1}. The asymmetric supercapacitor device using Ni-MOF/CNTs as the positive electrode delivers a high energy density of 36.6 Wh kg^{-1} at a power density of 480 W kg^{-1} with 95% specific capacitance retention after 5000 consecutive charge–discharge tests [13]. Sun and co-workers prepared few layer nanosheet $Ti_3C_2T_x$ by a solvothermal intercalation and exfoliation method for supercapacitor applications, which displayed a specific capacity of 508 F g^{-1} at a current density of 1 A g^{-1} and an energy density of 8.93 Wh kg^{-1} at a power density of 7.98 kW kg^{-1} with 90.3% capacity retention after 2000 charge–discharge cycles [14]. Although hydrothermal method is simple and effective, the high temperature required by hydrothermal method usually leads to uncontrollable growth of 2D MOF nanosheets with serious agglomeration which further inhibit its performance as an electrode material. The morphology, domain size and topological structure of the electrode materials are the key factors to affect the energy density of supercapacitor [15, 16]. Therefore, the development of controllable synthesis of reliable electrode materials with uniform morphology and appropriate topological structure is imperative.

In recent years, a class of bottom-up 2D MOF nanosheets can be synthesized directly from ionic and molecular compositions, allowing for the adjustment of morphology and microstructure of these 2D materials through the choice of component such as metal ions and organic ligands [17–19]. Thus it is a controllable synthesis. In addition, such 2D MOF nanosheets have good chemical stability. Wong and co-workers fabricated a bis(terpyridine)-Co(II) complex nanosheet with rich electrochemical activity, which showed good stability both in air and in solution [20]. Because of the excellent complexation ability towards different metal ions such as Co^{2+}, Zn^{2+}, Ni^{2+} etc., terpyridine has been extensively used as a tridentate ligand to construct various 2D nanomaterials [21]. Furthermore, it is worth pointing out that reports on 2D MOF nanosheets by hydrothermal method are very common, but bottom-up 2D nanosheets fabricated by liquid–liquid (L–L) interfacial-assisted method and used for electrodes are still rare.

In view of the above considerations, through a simple interface-assisted method, a tris(terpyridine) ligand-based metal coordination nanosheet Co-TPY-LB has been successfully synthesized, which has a layered structure with a thickness of 83.3 nm and displays a high utilization rate of redox active sites, good electrochemical stability and energy storage performance. The highest capacity of 2741.5 F g^{-1} at the current density of 1 A g^{-1}, and an excellent cycling stability with 97.6% capacity retention after 1000 cycles was achieved for electrode Co-TPY-LB. Meanwhile, the assembled asymmetric supercapacitor with Co-TPY-LB as the positive electrode shows a high energy density of 73.6 Wh kg^{-1} at a power density of 4800 W kg^{-1} as well as an excellent cycle stability of 92.9% capacity retention after 5000 cycles.

2 Experimental

2.1 Chemicals and Reagents

All chemical reagents were analytically pure and were used directly without purification or treatment. Cobalt(II) nitrate hexahydrate ($Co(NO_3)_2{\cdot}6H_2O$, > 99.0%), ethanol (CH_3CH_2OH, AR, 95%), dichloromethane (CH_2Cl_2, > 99.9%), N,N-dimethylformamide (DMF, AR, ≥ 99.9%), potassium hydroxide (KOH, 95%), and 1,3,5-tris(4'-tripyridinylphenyl)-benzene (Tris-tpy, 95%) were obtained from Shanghai Titan Scientific Co., Ltd. The water used for the preparation of the solution was deionized water.

2.2 Synthesis of Nanosheet Co-TPY-LB and Bulk Co-TPY-HT

First, a CH_2Cl_2 solution of the ligand Tris-tpy (10 mL, 4.0×10^{-5} mol L^{-1}) was degassed and then poured into a glass vial with a volume of 50 mL and a diameter of 3.2 cm. Solutions were then covered with 10 mL of degassed deionized water to form a buffer layer before the addition of 10 mL water solution of $Co(NO_3)_2{\cdot}6H_2O$ (5.0×10^{-2} mol L^{-1}). The reactions were allowed to take place at room temperature for 3 days. After that, a golden-colored nanosheet emerged at the water/oil interface as layered solids, which were marked as Co-TPY-LB (Fig. 1). After the removal of the aqueous and organic solvents, the as-fabricated nanosheet was transferred to the substrates and washed thoroughly with deionized water, ethanol, and CH_2Cl_2, and dried in vacuo, respectively.

$Co(NO_3)_2{\cdot}6H_2O$ (1.16 g) was added to a 80 mL of degassed DMF solution of the ligand Tris-tpy (4×10^{-5} mol L^{-1}), and the mixed solution was then sonicated for 10 min. After that, the mixed solution was poured into a teflon-lined stainless steel autoclave (100 mL capacity) and heated for

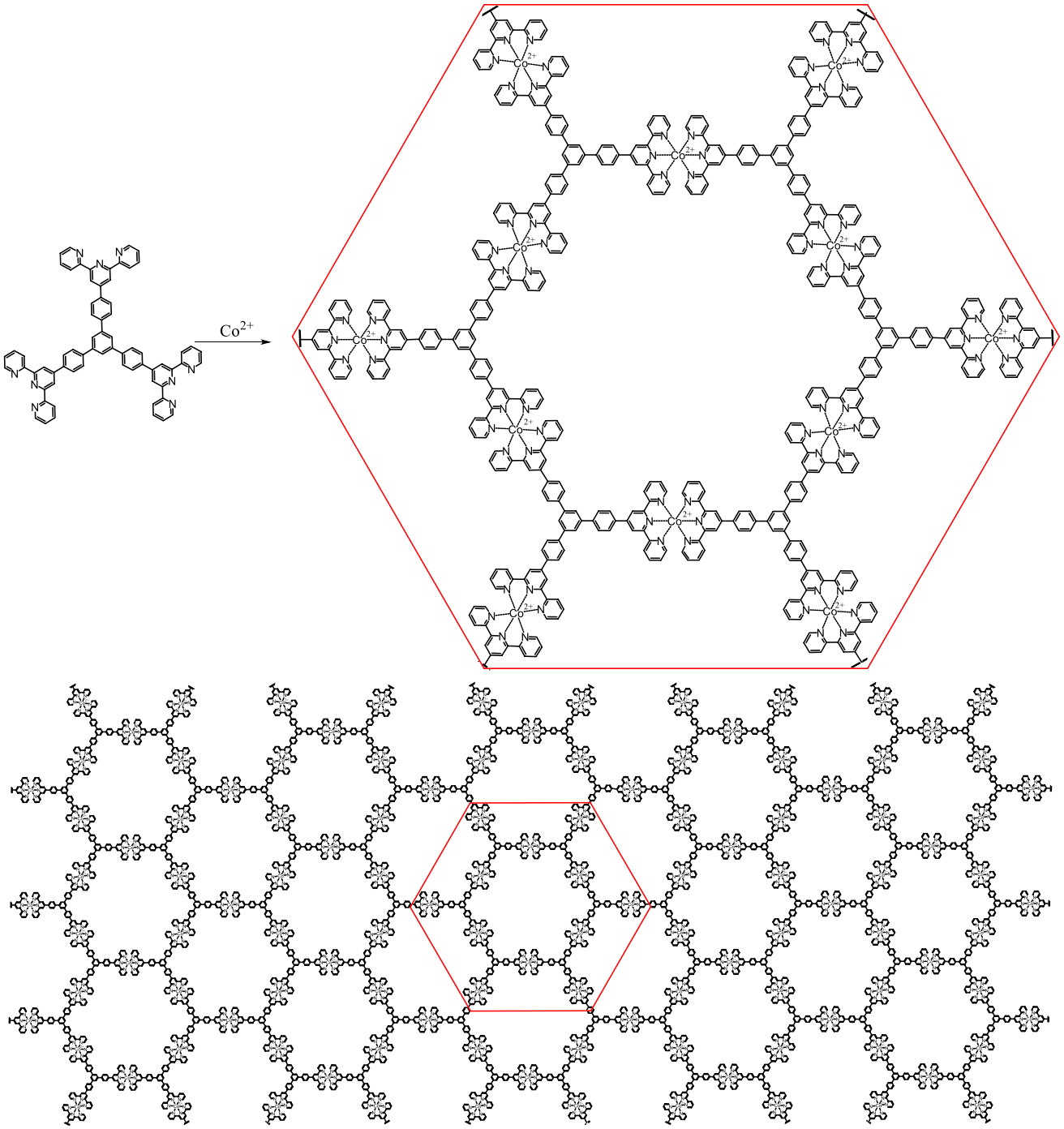

Fig. 1 Schematic illustration and chemical structure of nanosheet Co-TPY-LB derived from the coordination between Co^{2+} ion and ligand Tris-tpy

12 h at 160 °C. After being cooled to room temperature naturally, a black precipitate was obtained and thoroughly washed and centrifuged with deionized water, DMF and ethanol several times. Finally, the collected sample was placed in a vacuum oven at 60 °C and dried for 12 h. The as-fabricated sample was marked as Co-TPY-HT.

2.3 Physical Characterization

Scanning electron microscope and energy dispersive X-ray spectroscopy (SEM and EDX, Hitachi S-4800) were carried out to observe the morphologies and element distributions of nanosheet Co-TPY-LB at 1.0−2.0 kV and 10−20 kV,

respectively. Transmission electron microscopy and high resolution transmission electron microscopy (TEM and HRTEM, ThermoFischer FEI tecnai f20) were carried out to observe the morphologies of Co-TPY-LB with the accelerating voltage of 200 kV. Atomic force microscopy (AFM, Shimadzu SPM-9700) was carried out to observe the thickness of Co-TPY-LB. At the same time, X-ray photoelectron spectroscopy (XPS) was conducted under 30 eV Al-Kα radiation using ThermoFischer Escalab Xi^+. Infrared spectra (IR) were recorded on the Shimadzu IR Prestige-21 FT-IR spectrometer using KBr pellets for solid state spectroscopy. Powder X-ray diffraction (PXRD) was performed on a Bruker D8 Advance X-ray diffractometer, with Cu Kα1 (45 kV, 100 mA). The N_2 adsorption–desorption measurements were conducted with an ASAP2460 Surface Area and Porosity Analyzer at 150 ℃.

2.4 Fabrication and Characterization of Electrodes

Nickel (Ni) foam (the size of the electro-deposition is 2 cm × 1.5 cm) was soaked in acetone, deionized water and 0.1 mol L^{-1} HCl solution and placed under an ultrasonic cleaner for 10, 5 and 10 min, respectively. Then the Ni foam was dried for 3 h at 60 ℃ under vacuum after being cleaned repeatedly using deionized water and ethanol three times, respectively. The working electrode was prepared for Co-TPY-HT as follows: the acquired bulk Co-TPY-HT, acetylene black and polytetrafluoroethylene (PTFE) with a mass ratio of 8:1:1 were mixed with isopropanol to form a homogeneous slurry. Afterwards, the slurry was coated on an as-prepared Ni foam electrode. Finally, the electrode was allowed to dry at room temperature for 3 h. All the electrochemical studies were carried out under ambient conditions. The mass loadings of the electrodes NS1, NS2, NS3, NS4 and Co-TPY-HT on each substrate were 0.49, 0.72, 0.85, 0.96 and 2.1 mg respectively, which were calculated by the mass difference before and after the coating. All materials were weighed in a millionth high-precision analytical balance (Model: RADWAG XA 4Y.M.A).

All electrochemical properties such as cyclic voltammetry (CV), galvanostatic charge–discharge (GCD), electrochemical impedance spectroscopy (EIS) and long-term stability measurements were performed in a three-electrode system containing 1.0 M KOH aqueous solution as the electrolyte on a CHI 660E electrochemical workstation (CH Instruments, Chenhua. Co., Shanghai). The Ni foam modified with the as-fabricated nanosheet Co-TPY-LB or slurry containing Co-TPY-HT was used as the working electrode, a saturated calomel (SCE) electrode and a platinum sheet were applied as the reference electrode and the counter electrode, respectively. CV was measured within the potential window of 0 to 0.5 V at the scan rates of 2–50 mV s^{-1}. GCD curves were conducted in the potential range of 0–0.41 V at different constant current density with 1–10 A g^{-1}. The cycle life tests were carried out by GCD measurements with a constant current density of 10 A g^{-1} for 1000 cycles. EIS measurements were performed in the AC frequency range of 10^{-2}–10^5 Hz with an amplitude of 5 V using a 1 M KOH electrolyte solution.

The relationship of peak current (i) and sweep rate (v) can be described by the following formulas:

$$i = av^{b} \tag{1}$$

$$\log(i) = b\log(v) + \log(a) \tag{2}$$

where a and b are adjustable parameters. The value of b can be calculated from the slope of log(v) vs log(i). Generally, the value $b = 0.5$ indicates a diffusion-controlled process, while the value $b = 1$ implies a typical capacitive contribution.

In addition, the capacitance contribution at different scanning rates can be derived from the following formula:

$$i = k_1 v + k_2 v^{1/2} \tag{3}$$

where $k_1 v$ and $k_2 v^{1/2}$ reflect the surface-controlled process and diffusion-controlled process contribution, respectively.

The following formula is applied to calculate the electrode specific capacitance in the three-electrode configuration based on the GCD test data.

$$C_s = \frac{i_m \times \Delta t}{\Delta V} \tag{4}$$

where C_s is the specific capacitance (F g^{-1}), Δt is the discharge time (s), i_m is the current density (A g^{-1}), and ΔV is the potential window (V).

2.5 Fabrication and Characterization of Co-TPY-LB// AC Based Asymmetric Supercapacitor (ASC)

For evaluating the application prospect of the electrode, asymmetric supercapacitor (ASC) should be prepared. An asymmetric supercapacitor consists of the Co-TPY-LB electrode, AC, and 6 M KOH aqueous solution, which was employed as the positive electrode, negative electrode, and electrolyte, respectively. The negative electrode was prepared for AC according to the literature method as follows: the acquired AC, acetylene black and PTFE with a mass ratio of 8:1:1 were mixed in isopropanol to form a homogeneous slurry. Afterwards, the slurry was coated on an as-prepared Ni foam. Finally, the electrode was dried at room temperature for 4 h. The button battery shells and water-based diaphragms of the devices were purchased from the Self-Reliance Battery Sales Department. The model of the shell is LIR2016, which is made of 304 stainless steel, and the diameter and thickness

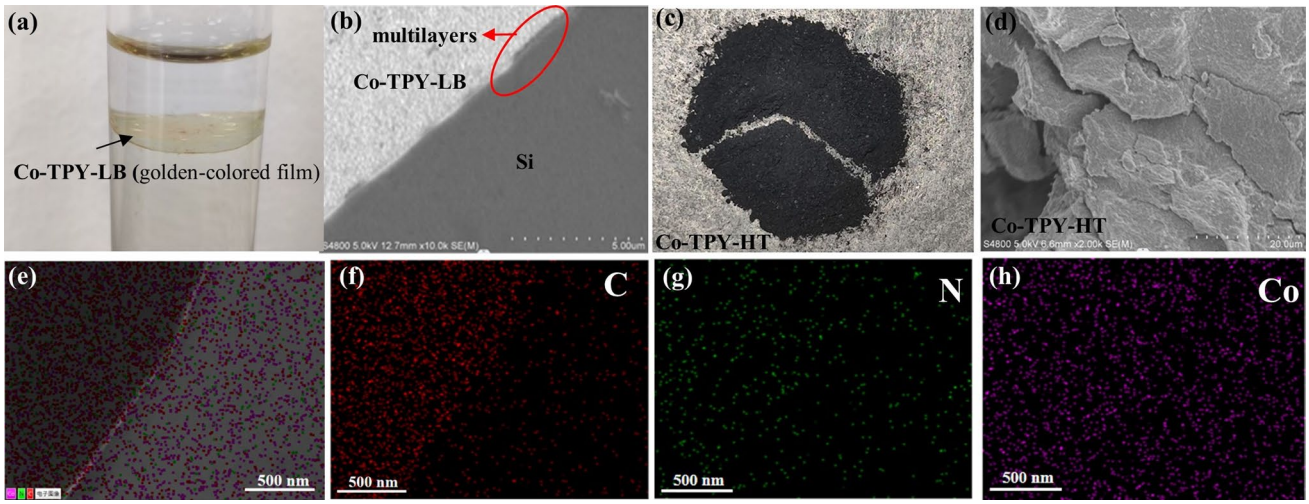

Fig. 2 **a** Photograph of Co-TPY-LB (gold film) at the liquid-liquid interface (the upper layer has been washed by deionized water several times). **b** The SEM image of nanosheet Co-TPY-LB deposited on Si substrate. **c** Photograph of Co-TPY-HT from the reaction by hydrothermal method. **d** The SEM image of referential complex Co-TPY-HT deposited on Si substrate. **e** The SEM/EDX of Co-TPY-LB on FTO substrate. The SEM/EDX mapping images of Co-TPY-LB for **f** C, **g** N and **h** Co, respectively

are 20 mm and 1.6 mm. The positive electrode is made of a Ni foam slice with 12 mm in diameter, which is loaded with nanosheet Co-TPY-LB and the area loading is about 0.12 mg cm^{-2}. The negative electrode is made of a Ni foam slice with 16 mm in diameter, which is loaded with AC. The water-based diaphragm is made of PP/PE, EVOH and special nylon fiber with a thickness of 150 µm, which is cut into a round piece with a diameter of 20 mm for the preparation of ASC device. About 0.3 mL 6 M KOH was used for the electrolyte. The mass loading of active materials used for positive and negative electrodes must abide the charge balance relationship (Q+ = Q−) based on the following formula:

$$\frac{M^+}{M^-} = \frac{C^- \times \Delta V^-}{C^+ \times \Delta V^+} \tag{5}$$

The energy and power density of the Co-TPY-LB //AC based ASC device could be obtained as follows:

$$E = \frac{1}{2} \times \frac{C_s \times V^2}{3.6} \tag{6}$$

$$P = \frac{3600E}{\Delta t} \tag{7}$$

where E is the energy density (Wh kg^{-1}), P is the power density (W kg^{-1}), C_s is the specific capacitance (F g^{-1}), V is the voltage and Δt is the discharge time (s).

3 Results and Discussion

3.1 Structure and Morphology for Nanosheet Co-TPY-LB

Through a L-L interfacial-assisted method, the ligand Tris-tpy with three functional terpyridine groups could spontaneously coordinate with Co^{2+} to obtain the nanosheet Co-TPY-LB with the polymeric structure depicted in Fig. 1 (the counter anions are omitted for clarity). As shown in Fig. 2a, a spontaneous reaction produced the nanosheet Co-TPY-LB at the oil/water interface, which resulted in a golden-colored film. Nanosheet Co-TPY-LB was insoluble in water and any organic solvents, which can be easily transferred from the interface onto various substrates, such as Si, Ni foam and fluorine-doped tin oxide (FTO) substrates. SEM image was conducted to show a flat, layered structure for nanosheet Co-TPY-LB (Fig. 2b). A layer-by-layer stacking pattern of the bottom-up growth was announced by the multilayer structure on the edge. For the purpose of a contrast analysis, a conventional hydrothermal method was used to synthesize Co-TPY-HT (Fig. 2c). Far from the film texture of nanosheet Co-TPY-LB, Co-TPY-HT exhibited a disordered and irregular block structure (Fig. 2d). Besides the SEM technique, EDX was conducted for nanosheet Co-TPY-LB to detect the elemental composition and distribution. The homogeneity in the distribution of Co and N for Co-TPY-LB

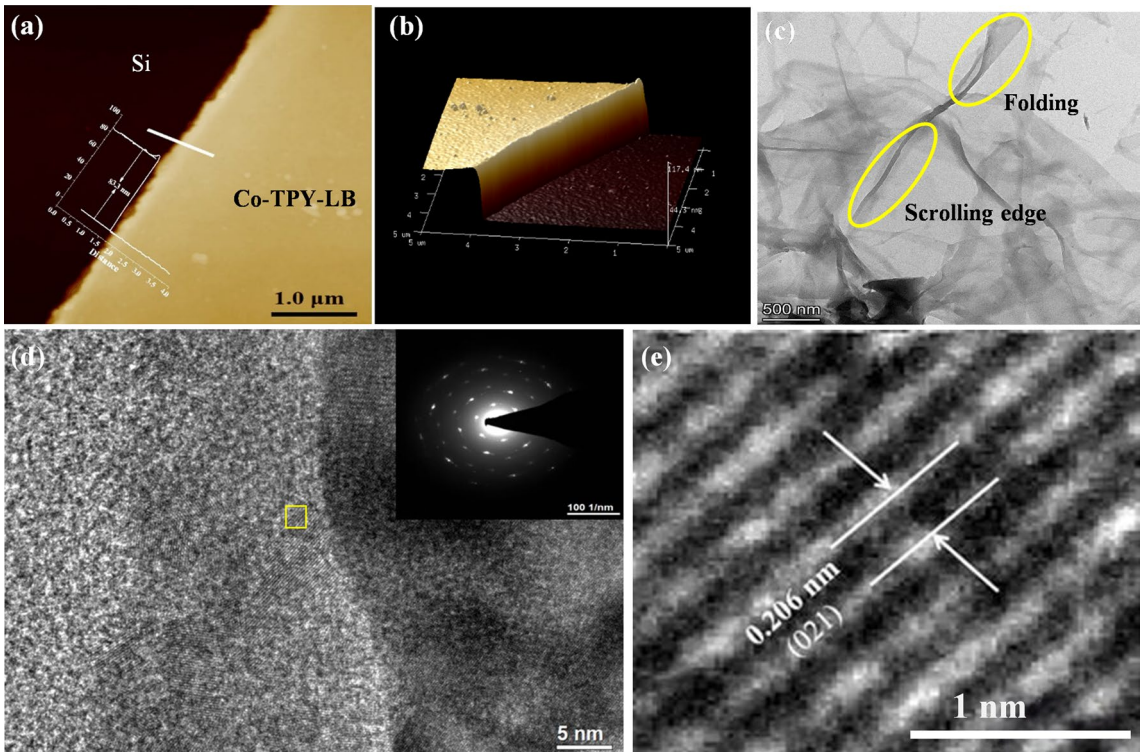

Fig. 3 **a** The AFM image of the nanosheet Co-TPY-LB and the cross-sectional analysis along with the white line. **b** The 3D AFM image of nanosheet Co-TPY-LB. **c** TEM and **d** HRTEM image for Co-TPY-LB on ultrathin pure carbon film with no formvar backing on lacey carbon support film. **e** The lattice distance of hexagonal structure shown in the yellow square in **d**

as proposed can be revealed by the SEM/EDX mapping images (Fig. 2e–h). The ratio of N:Co is 6.52:1, which agrees with the ideal stoichiometric value (6:1) (Fig. S1), indicating the successful coordination of pyridine and Co^{2+} ion, which is in accordance with the schematic illustration in Fig. 1. FT-IR spectra of ligand Tris-tpy and nanosheet Co-TPY-LB are shown in Fig. S2. The peaks at 1645, 1386 and 1286 cm^{-1} for nanosheet Co-TPY-LB can be assigned to aromatic C = C, C = N and C–N stretching, respectively, which are all shifted compared with that of ligand Tris-tpy, indicating the metal coordination behaviour. Meanwhile, the appearance of a new absorption band for Co–N stretching at 460 cm^{-1} is a further proof of the coordination between Co^{2+} ion and the nitrogen of terpyridine group [22]. PXRD was conducted for nanosheet Co-TPY-LB to investigate the crystallinity and phase purity (Fig. S3). Nanosheet Co-TPY-LB displayed a strong diffraction peak at the 2θ value of 44.5°, which is attributed to the (021) plane and in line with the result of HRTEM results (vide infra). Furthermore, the AFM image of nanosheet Co-TPY-LB revealed a flat and smooth sheet structure with a thickness of 83.3 nm (Fig. 3a), and an excellent and flat morphology coverage on the Si substrate for Co-TPY-LB was demonstrated by the three dimensional AFM image (Fig. 3b). In order to study the detailed structure of the nanosheet Co-TPY-LB, the TEM and HRTEM techniques were further applied. TEM image of the Co-TPY-LB shows a typical film-like structure with a thin and transparent morphology (Fig. 3c). The folding and scrolling texture is recognized as the evidence of sheet material. Due to the (021) plane and in agreement with the result of PXRD study, the HRTEM image shows that nanosheet Co-TPY-LB owns a hexagonal structure with a lattice spacing of about 0.206 nm (Fig. 3d,e), which provides a large number of redox sites and ion diffusion channels. The selected-area electron diffraction demonstrates the polycrystalline structure of nanosheet Co-TPY-LB (inset of Fig. 3d).

Furthermore, XPS was conducted to study the internal structure and electronic surface state of ligand Tris-tpy, Co-TPY-LB, and bulk Co-TPY-HT (Fig. 4 and Fig. S4). The peaks related to C 1s, N 1s, O 1s and Co 2p of Co-TPY-LB are shown in the XPS spectra (Fig. 3a and Fig. S4b), and the presence of oxygen element probably arises from the air atmosphere. Compared with the referential ligand Tris-tpy (Fig. S4a), an additional Co 2p peak appeared for nanosheet Co-TPY-LB, which is the evidence of the successful coordination between Co^{2+} ions and ligand Tris-tpy. As shown in Fig. 4b, the narrow XPS spectra of Co-TPY-LB focusing on Co 1 s prove that the valence state of Co ions in Co-TPY-LB is only +2. Compared with nanosheet Co-TPY-LB, there are two valence states of +2 and +3 for

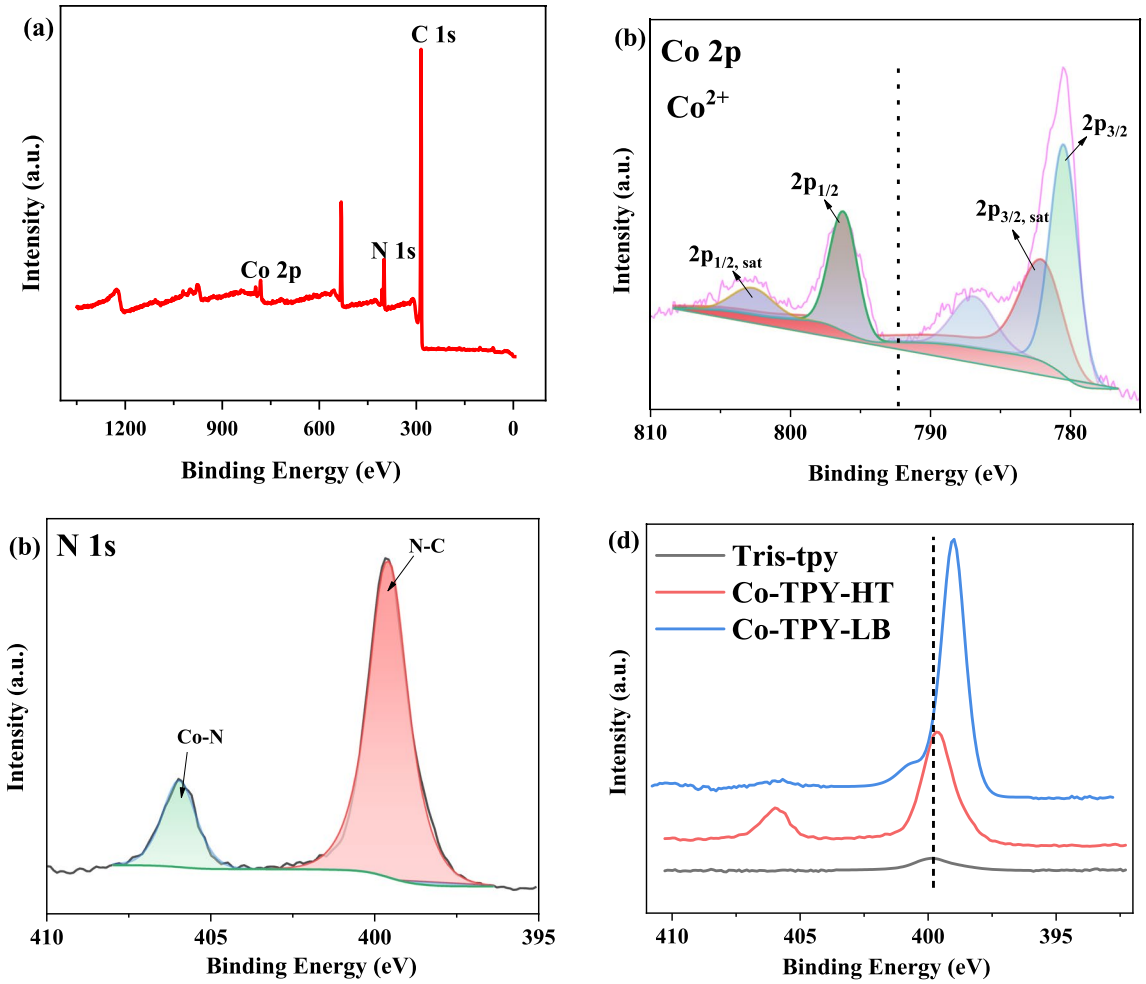

Fig. 4 The full XPS spectrum of **a** Co-TPY-LB. The narrow XPS spectra of Co-TPY-LB focusing on **b** Co 2p and **c** N 1s, respectively. **d** The narrow scan XPS spectra of nanosheet Co-TPY-LB, bulk Co-TPY-HT and ligand Tris-tpy focusing on N 1s core level

Co ions in bulk Co-TPY-HT (Fig. S4d), which could be attributed to the fact that high temperature and pressure for hydrothermal synthesis make the reactants to form clusters easily, leading to the oxidation of some original Co^{2+} ions to Co^{3+} ions. As shown in Fig. 3b, the binding energies at 780.6 eV and 796.3 eV correspond to the Co 2p3/2 and Co 2p1/2 peaks for Co^{2+}, respectively [23, 24]. Additionally, the two satellite (sat.) peaks appeared at 802.8, 782.9 eV correspond to the Co^{2+} after the chemical reaction between the coordination of Co^{2+} with terpyridine group from the Tris-tpy [25]. Due to the Co–N and the C–N bonds in nanosheet Co-TPY-LB, the N 1s spectrum of Co-TPY-LB is splitted into two peaks at 399.5 and 398.0 eV respectively (Fig. 4c), demonstrating the successful coordination between Co^{2+} ions and ligand Tris-tpy [26]. Figure 4d shows the narrow XPS spectra focusing on the N 1s for ligand Tris-tpy, nanosheet Co-TPY-LB and bulk Co-TPY-HT. The peak of N 1s shifted between Tris-tpy (399.9 eV) and Co-TPY-LB (399.0 eV), indicating the functional terpyridine group of Tris-tpy reacted with Co^{2+} ions to result in the nanosheet Co-TPY-LB. In addition, the disappearance of the shoulder peaks for N 1s is the reflection of the completion of coordination [19]. In addition, the binding energy of N 1s core level is 399.6 eV for bulk Co-TPY-HT, which is very close to that of nanosheet Co-TPY-LB, further providing the evidence for the formation of the Co(II)-N moieties within Co-TPY-LB. Brunauer–Emmett–Teller (BET) tests were carried out for both nanosheet Co-TPY-LB and hydrothermal method made bulk counterpart Co-TPY-HT (Fig. S5) to study their adsorption–desorption behaviour. The specific surface area of Co-TPY-LB is calculated to be 16.27 $m^2\ g^{-1}$, which is about three times higher than that of Co-TPY-HT (5.54 $m^2\ g^{-1}$). Presumably it is because that the bottom-up synthesis method with ambient temperature and pressure is more conducive to form a superstructure with ordered nanopores and layered structure.

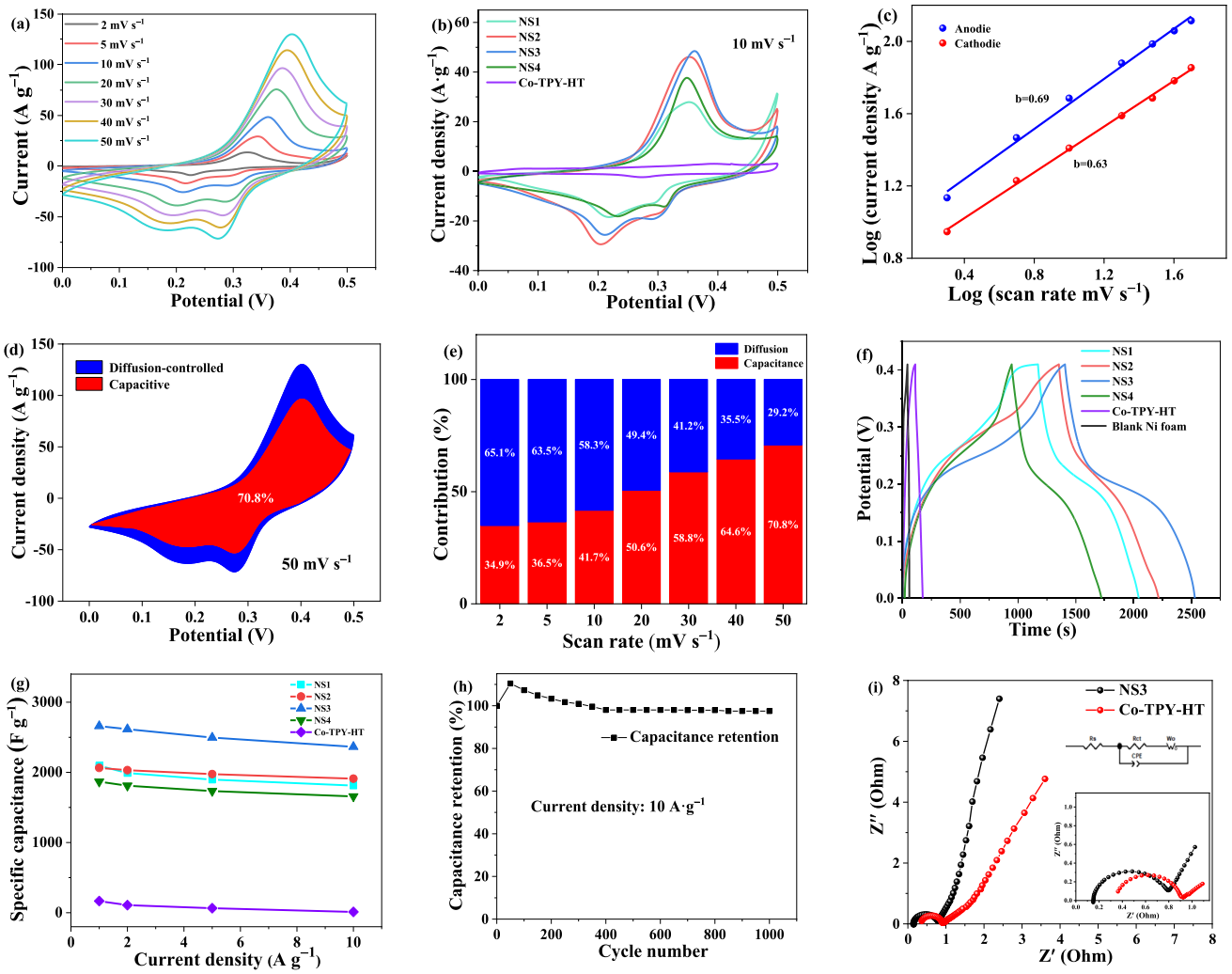

Fig. 5 **a** CV curves of electrode NS3 at different scan rates from 2 to 50 mV s^{-1}. **b** The CV curves of various electrodes at the scan rate of 10 mV s^{-1}. **c** The *b*-value determination of the peak anodic and cathodic currents for electrode NS3. **d** Capacitance contribution at a scan rate of 50 mV s^{-1} for electrode NS3. **e** Contribution of capacitive and diffusion-controlled percentages at different scan rates from 2 to 50 mV s^{-1} for electrode NS3. **f** The GCD curves of various electrodes at 1 A g^{-1}. **g** Specific capacitance curves of various electrodes at different current densities. **h** Cycling performance of the electrode NS3 in the potential range of 0–0.41 V at 10 A g^{-1}. **i** Comparison of the EIS Nyquist plots for electrodes NS3 and Co-TPY-HT. Inset: the high-frequency region data for (**i**)

3.2 Electrochemical Performance of Electrodes Co-TPY-LB and Co-TPY-HT

Since the layered structure with ordered nanopores and lattice spacing can provide a large number of redox sites and ion diffusion channels, the as-fabricated nanosheet Co-TPY-LB is expected to have good electrochemical properties. In order to prove the superiority of bottom-up nanosheets in electrochemical performances, nanosheet Co-TPY-LB and bulk Co-TPY-HT by hydrothermal method were prepared and studied as positive electrodes, in which electrodes Co-TPY-LB with mass loadings of 0.49, 0.72, 0.85 and 0.96 mg were marked as electrodes NS1, NS2, NS3 and NS4, respectively. In a three-electrode system containing 1.0 M KOH aqueous solution, cyclic voltammetry (CV), galvanostatic charge–discharge (GCD), electrochemical impedance spectroscopy (EIS) and long-term stability measurements were conducted to evaluate the electrochemical performances of the electrodes. The CV performance of the electrodes NS1–NS4 and electrode Co-TPY-HT at different scan rates from 2 to 50 mV s^{-1} are depicted in Fig. 5a and Fig. S6, respectively. There are obvious redox peaks on the CV curves of all the electrodes NS1–NS4, indicating that the pseudocapacitance behavior is caused by the faradaic redox reactions on the surface of the electrodes. The oxidation states and the possible conversion of cobalt

Table 1 Discharge times and specific capacitance for electrodes NS1–NS4 and Co-TPY-HT with current densities of 1, 2, 5 and 10 A g^{-1}

Current density (A g^{-1})	Discharge time (s)					Specific capacitance (F g^{-1})				
	NS1	NS2	NS3	NS4	Co-TPY-HT	NS1	NS2	NS3	NS4	Co-TPY-HT
1	858.5	846.1	1105.1	765.4	76.1	2093.8	2063.7	2741.5	1866.8	185.6
2	408.1	416.4	549.3	380.1	24.7	1990.6	2031.2	2679.5	1854.1	120.5
5	155.6	161.9	209.6	145.6	5.9	1896.3	1974.4	2556.1	1775.6	71.9
10	74.3	78.3	99.3	69.6	0.5	1812.2	1909.8	2421.9	1697.5	12.2

in the possible charge storage mechanism are expressed as: $Co(II)_s + OH^- \rightleftharpoons Co(II)(OH)_{ad} + e^-$and $Co(II)(OH)_{ad} \rightleftharpoons Co(III)(OH)_{ad} + e^-$, where s and ad represent the solid and adsorption state, respectively [27].

As shown in Fig. 5a and Fig. S6, as the scan rate increases, the area of all the CV curves and its peak value of the current density both increase significantly, demonstrating that rapid ion absorption and diffusion occurs in the electrodes and is conducive to a fast and reversible Faradaic reaction. Compared with the electrode Co-TPY-HT, electrodes NS1–NS4 own higher integrated surface areas in the potential window of 0 to 0.5 V at the scan rate of 10 mV s^{-1} (Fig. 5b), suggesting that the specific capacitances of electrodes NS1–NS4 fabricated by bottom-up method are much better than that of electrode Co-TPY-HT fabricated by solvothermal method.

To further explore the storage kinetics of the electrodes NS1–NS4, CV profiles of the NS1–NS4 anode at different scanning rates from 2 to 50 mV s^{-1} were recorded. As shown in Fig. 5a and Fig. S6a-c, the shape of CV curves for the NS1–NS4 does not change significantly with the increase of scan rate. According to formulas (1) and (2), the *b* values of the anodic and cathodic peaks are 0.69 and 0.63, indicating a predominant capacitive contribution of NS3 (Fig. 5c) [28]. Furthermore, According to formula (3), the capacitive contribution for the electrode NS3 accounts for 70.8% of the total capacitance at 50 mV s^{-1} (Fig. 5d). As the scan rate increases from 2 to 50 mV s^{-1}, the capacitance contribution gradually increased from 34.9 to 70.8%, indicating mainly being dominated by Faradaic pseudocapacitive behaviour rather than diffusion-controlled process (Fig. 5e).

GCD curves of electrodes NS1–NS4, Co-TPY-HT and blank Ni foam at the different current densities from 1 to 10 A g^{-1} within the potential range of 0 to 0.41 V are shown in Fig. S7, which indicates that the electrodes NS1–NS4 have excellent electrochemical performance. The shapes of charge–discharge curves are consistent with the characteristics of CV curve mentioned above, thus the fact that the nanosheet Co-TPY-LB can be used as electrode materials for pseudocapacitive supercapacitors can be also proved. Under the current density of 1 A g^{-1}, the discharge times are 858.5, 846.1, 1105.1 and 765.4 s for electrodes NS1–NS4, but only 76.1 s for electrode Co-TPY-HT (Fig. 5f, Table 1). According to the calculation of formula (4), the specific capacitance values of 2093.8, 2063.7, 2741.5 and 1866.8 F g^{-1} have been reached for the electrodes NS1–NS4 at the current density of 1 A g^{-1}, respectively (Table 1), which are higher than many other reported electrode materials, such as CNT@MOFs [29], NiCo-MOF [30], Co-MOF [31], and Cu-DBC [32]. Under the same test conditions, the discharge time for blank Ni foam is 16.4 s and the value of specific capacitance is only 40 F g^{-1}, which is far smaller than that of electrodes NS1–NS4, thus the specific capacitance of blank Ni foam can be negligible. Comparatively, the specific capacitance value of electrode Co-TPY-HT is only 185.6 F g^{-1}, which is far lower than that of electrodes NS1–NS4. Benefiting from the layered structure with ordered nanopores and lattice spacing of nanosheet Co-TPY-LB, a large number of redox sites and ion diffusion channels can be provided and the conductivity and the electrochemical behavior have been improved, thus the electrodes NS1–NS4 show greater potential for efficient electrochemical energy storage than that of electrode Co-TPY-HT [33, 34]. Meanwhile, when the current density increases, the capacitance retention ratio of electrodes NS1–NS4 are as high as 86.8%, 92.5%, 88.3% and 90.9%, respectively, reflecting the good rate capability of electrodes NS1–NS4 under different current densities (Fig. 5g). In addition, a good reversibility and stability for electrodes NS1–NS4 can be proved by the good symmetry under different current densities of 1 to 10 A g^{-1}. In order to examine the cyclic performance of nanosheet Co-TPY-LB, GCD test of 1000 cycles were conducted for electrode NS3 at 10 A g^{-1} in the potential range of 0 to 0.41 V, and an excellent cycling stability with a capacitance retention of 97.6% after 1000 cycles was presented (Fig. 5h). Due to the activation process in the initial cycle process, a significant upward trend for the specific capacitance is shown and 110.4% of the initial specific capacitance can be obtained in the first 50th cycles. From the 500th cycle to the 1000th cycle, there is almost no change in specific capacitance, only a decrease of 0.4% can be observed, demonstrating the electrode material Co-TPY-LB is stable. The EIS Nyquist plot for electrode NS3 is composed of a tiny semicircle in the high frequency region

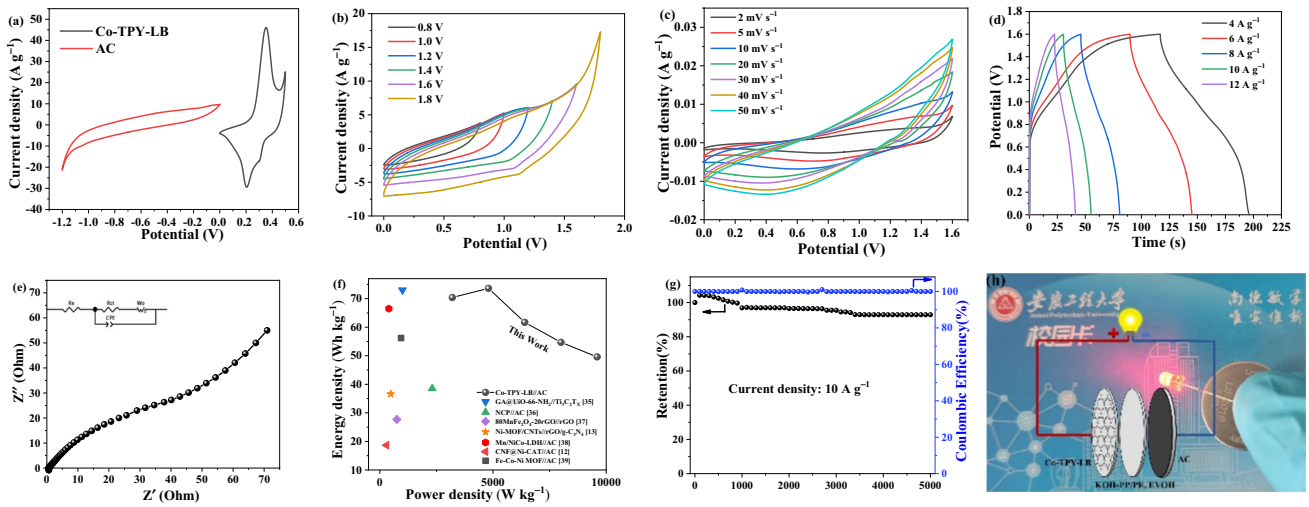

Fig. 6 **a** Comparison of CV curves between electrodes Co-TPY-LB and AC at 2 mV s^{-1}. **b** CV curves of the as-assembled ASC device tested with different potential windows. **c** CV curves of the as-assembled ASC device at different scan rates from 2 to 50 mV s^{-1}. **d** GCD curves with different current densities from 4 to 12 A g^{-1}. **e** EIS Nyquist plot of the as-assembled ASC device. **f** Comparison of energy density and power density of the as-assembled ASC device with other reported ASC electrode materials. **g** Cycling stability and coulombic efficiency of the as-assembled ASC device at the current density of 10 A g^{-1} after 5000 charge–discharge cycles. **h** Schematic diagram and photograph of the yellow LED lighting up by the as-assembled ASC device

and a straight line in the low frequency region (Fig. 5i). A small electrolyte resistance (R_s) of 0.15 Ω for electrode NS3 indicates the excellent charge transfer performance, which is also proved by the small charge-transfer resistance (R_{ct} = 0.64 Ω). Comparatively, the values of R_s for electrode Co-TPY-HT is 0.36 Ω, indicating a relatively lower charge transfer than that of electrode NS3. The inclination angle of the curve of electrode NS3 is much greater than that of electrode Co-TPY-HT in the low frequency region, which indicates the better ion mobility for NS3. This may be attributed to the layered structure of electrode material Co-TPY-LB with ordered nanopores and lattice spacing, which is conducive to the migration of OH^-.

3.3 Asymmetric supercapacitor (ASC) performance based on Co-TPY-LB//AC (active carbon)

To investigate the practical application of such bottom-up nanosheet, Co-TPY-LB was used as positive electrode and AC was used as negative electrode to assemble the ASC device. The CV curves of Co-TPY-LB and AC at the scan rate of 2 mV s^{-1} are shown in Fig. 6a. CV curves of the ASC device with different potential windows are shown in Fig. 6b at the scan rate of 50 mV s^{-1}. Conspicuous polarization peak was observed within 1.6 ~ 1.8 V, suggesting an appropriate working potential window of 1.6 V is appropriate for the Co-TPY-LB//AC based ASC device. The rectangular shape with the broad redox peaks of the CV curves indicates the charge storage is the integration of pseudocapacitance and double-layer capacitance [35]. Meanwhile, the shape of the CV curves was maintained well from 2 ~ 50 mV s^{-1}, demonstrating a fast charge–discharge performance for the as-assembled ASC device [36]. The as-assembled ASC device shows a specific capacitance of 198, 207, 173.5, 153.8 and 139.5 F g^{-1} at a current density of 4, 6, 8, 10 and 12 A g^{-1}, respectively, delivering a good rate capability of 70.3%. The EIS plot for the as-assembled ASC device exhibits a very low R_s of 0.65 Ω in the high frequency region and a straight line over 45° in the low frequency region, which indicate a low charge transfer resistance and ion diffusion resistance are favorable for the ions to approach the active center, enabling that nanosheet Co-TPY-LB is good for high specific energy storage devices [37]. According to the calculation based on formulas (6) and (7), the as-assembled ASC device shows a maximum energy density of 73.6 Wh kg^{-1}@4800 W kg^{-1} and a maximum power density of 49.6 Wh kg^{-1}@9600 W kg^{-1} (Fig. 6f, Table 2), which

Table 2 Specific capacitance, energy density and power density of Co-TPY-LB//AC based ASC at different current densities

Current density (A g^{-1})	Specific capacitance (F g^{-1})	Energy density (Wh kg^{-1})	Power density (W kg^{-1})
4	198	70.4	3200
6	207	73.6	4800
8	173.5	61.7	6401
10	153.8	54.7	8005
12	139.5	49.6	9600

are equivalent to or much higher than previously reported state-of-the-art ASC electrode materials [12, 13, 38–42]. About 92.9% of their original capacitance was retained after 5000 continuous cycles along with a coulombic efficiency of nearly 100%, indicating an excellent cycling durability for the as-assembled ASC device. To test the practical applicability of our low-cost button-type ASC device manufactured on the laboratory scale, a simple circuit device was made and the yellow LED can be easily lighted up (Fig. 6h).

4 Conclusion

In this contribution, a tris(terpyridine) ligand-based metal coordination nanosheet Co-TPY-LB has been successfully synthesized by a simple interface-assisted method. The structure of the as-fabricated nanosheet Co-TPY-LB has been identified by FT-IR, PXRD, and the morphology has been revealed by SEM, AFM, TEM and HRTEM, which have a layered structure with a thickness of 83.3 nm. Compared with the corresponding bulk sample Co-TPY-HT, nanosheet Co-TPY-LB displays a high utilization rate of redox active sites, good electrochemical stability and energy storage performance, demonstrating the advantages of MOF nanosheet prepared by L-L interface assisted method. Electrodes NS1–NS4 have been fabricated by nanosheet Co-TPY-LB, which exhibit excellent capacities of 2093.8, 2063.7, 2741.5 and 1866.8 F g^{-1} at the current density of 1 A g^{-1} respectively, and an excellent cycling stability with 97.6% capacity retention after 1000 cycles for electrode NS3. The as-assembled ASC device with Co-TPY-LB as the positive electrode shows a high energy density 73.6 kW kg^{-1} at a power density of 4800 Wh kg^{-1} as well as an excellent cycle stability of 92.9% capacity retention after 5000 charge–discharge cycles. Our work provides a controllable synthesis for the construction of 2D metal coordination nanosheet to overcome some defects of 2D nanosheet by traditional synthesis, leading such bottom-up nanosheet to a promising application in energy storage.

Supplementary Information The online version contains supplementary material available at https://doi.org/10.1007/s10904-024-03165-6.

Acknowledgements Q.L. thanks the National Natural Science Foundation of China (51803002), Natural Science Foundation of Anhui Province (1708085QE93), Open Fund of Anhui Laboratory of Functional Coordinated Complexes for Materials Chemistry and Application (LFCCMCA-04), Anhui Provincial Demonstration Course Project "English for Science and Technology" (2022qyw/sysfkc024). W.Y.W. is grateful to the financial support from the Hong Kong Research Grants Council (PolyU 15307321), the RGC Senior Research Fellowship Scheme (SRFS2021-5S01), Research Institute for Smart Energy (CDAQ) and Miss Clarea Au for the Endowed Professorship in Energy (847S).

Author contributions Qian Liu: Conceptualization, Methodology, Writing – original draft, Project administration, Writing – review and editing. Zhiwei Xu: Investigation, Formal analysis, Resources. Zengqi Guo: Investigation, Data curation. Su Guo: Investigation. Mengru Huang: Data curation, Resources. Wai-Yeung Wong: Editing draft, Formal analysis, Supervision.

Funding Open access funding provided by The Hong Kong Polytechnic University This work was funded by National Natural Science Foundation of China (51803002), Natural Science Foundation of Anhui Province (1708085QE93), Open Fund of Anhui Laboratory of Functional Coordinated Complexes for Materials Chemistry and Application (LFCCMCA-04), Anhui Provincial Demonstration Course Project "English for Science and Technology" (2022qyw/sysfkc024), the Hong Kong Research Grants Council (PolyU 15307321), the RGC Senior Research Fellowship Scheme (SRFS2021-5S01), Research Institute for Smart Energy (CDAQ) and Miss Clarea Au for the Endowed Professorship in Energy (847S).

Declarations

Conflict of interest The authors confirm that this article content has no conflict of interest.

References

1. Y. Wang, T. Guo, E. Alhajji, Z. Tian, Z. Shi, Y.-Z. Zhang, Adv. Energy Mater. **13**, 2202860 (2023)
2. J. Yan, M.A. Baird, D.C. Popple, A. Zettl, T.P. Russell, B.A. Helms, J. Am. Chem. Soc. **144**, 3979–3988 (2022)
3. M. Pastore, S. Caramori, P.C. Gros, Acc. Chem. Res. **57**, 439–449 (2024)
4. Q. Liu, C. Wang, C. Hu, M. Wang, C. Li, Z. Guo, Y. Liu, W.-Y. Wong, J. Organomet, Chem. **960**, 122220 (2022)
5. B. Li, N. Hu, Y. Su, Z. Yang, F. Shao, G. Li, C. Zhang, Y. Zhang, ACS Appl. Mater. Interfaces **11**, 46044–46053 (2019)
6. T. Liu, R. Yan, H. Huang, L. Pan, X. Cao, A. de Mello, M. Niederberger, Adv. Funct. Mater. **30**, 2004410 (2020)
7. D. Feng, T. Lei, M.R. Lukatskaya, J. Park, Z. Huang, M. Lee, L. Shaw, S. Chen, A.A. Yakovenko, A. Kulkarni, J. Xiao, K. Fredrickson, J.B. Tok, X. Zou, Y. Cui, Z. Bao, Nat. Energy **3**, 30–36 (2018)
8. D. Sheberla, J.C. Bachman, J.S. Elias, C.-J. Sun, Y. Shao-Horn, M. Dincă, Nat. Mater. **16**, 220–225 (2017)
9. G. Wang, L. Zhang, J. Zhang, Chem. Soc. Rev. **41**, 797–828 (2012)
10. K. Tao, X. Han, Q. Cheng, Y. Yang, Z. Yang, Q. Ma, L. Han, Chem. Eur. J. **24**, 12584–12591 (2018)
11. H.T.B. Pham, J.Y. Choi, M. Stodolka, J. Park, Acc. Chem. Res. **57**, 580–589 (2024)

12. S. Zhao, H. Wu, Y. Li, Q. Li, J. Zhou, X. Yu, H. Chen, K. Tao, L. Han, Inorg. Chem. Front. **6**, 1824–1830 (2019)
13. P. Wen, P. Gong, J. Sun, J. Wang, S. Yang, J. Mater. Chem. A **3**, 13874–13883 (2015)
14. H. An, S. Wang, K. Liu, F. Zhang, S. Liang, X. Wang, N. Li, J. Xiao, X. Zhao, S. Li, Z. Sun, Colloid Interface Sci. **50**, 100650 (2022)
15. R.R. Salunkhe, Y.V. Kaneti, Y. Yamauchi, ACS Nano **11**, 5293–5308 (2017)
16. L. Wang, D. Shao, J. Guo, S. Zhang, Y. Lu, J. Solid State Chem. **277**, 630–635 (2019)
17. R. Sakamoto, K. Hoshiko, Q. Liu, T. Yagi, S. Kusaka, W.-Y. Wong, H. Nishihara, Nat. Commun. **6**, 6373 (2015)
18. R. Sakamoto, T. Yagi, K. Hoshiko, S. Kusaka, R. Matsuoka, H. Maeda, Z. Liu, Q. Liu, W.-Y. Wong, H. Nishihara, Angew. Chem. Int. Ed. **56**, 3526–3530 (2017)
19. Q. Liu, Z. Guo, C. Wang, S. Guo, Z. Xu, C. Hu, Y. Liu, Y. Wang, J. He, W.-Y. Wong, Adv. Sci. **10**, 2207545 (2023)
20. Y. Liu, W. Deng, Z. Meng, W.-Y. Wong, Small **16**, 1905204 (2020)
21. B.Z. Momeni, N. Davarzani, J. Janczak, N. Ma, A.S. Abd-El-Aziz, Coord. Chem. Rev. **506**, 215619 (2024)
22. Y. Liang, J. Wei, Y. Hu, X. Chen, J. Zhang, X. Zhang, S. Jiang, S. Tao, H. Wang, Nanoscale **9**, 5323–5328 (2017)
23. J. Park, M. Lee, D. Feng, Z. Huang, A.C. Hinckley, A. Yakoyenko, X. Zou, Y. Cui, Z. Bao, J. Am. Chem. Soc. **140**, 10315–10323 (2018)
24. H. Yu, S. Xie, J. Yang, W. Tan, J. Yin, J. Wang, M. Zhao, C. Wang, M. Zhao, G. He, L. Yang, Colloid. Surface A **645**, 128953 (2022)
25. B.K. Martin, L.S. Bezerra, S. Artemkina, V. Fedorov, P.K. Boruah, M.R. Das, G. Maia, Chem. Eng. J. **9**, 100206 (2022)
26. D. Cheng, Y. Zhao, X. Tang, T. An, X. Wang, H. Zhou, D. Zhang, T. Fan, Carbon **149**, 750–759 (2019)
27. X. Liu, C. Shi, C.W. Zhai, M.L. Cheng, Q. Liu, G. Wang, ACS Appl. Mater. Interfaces **8**, 4585–4591 (2016)
28. X. Liu, P. Geng, G. Zhang, Y. Zhang, F. Dou, H. Pang, Inorg. Chem. **62**, 6527–6536 (2023)
29. M. Lu, G. Wang, X. Yang, B. Hou, Nano Res. **15**, 6112–6120 (2022)
30. Y. Wang, Y. Liu, H. Wang, W. Liu, Y. Li, J. Zhang, H. Hou, J. Yang, ACS Appl. Energy Mater. **2**, 2063–2071 (2019)
31. W. Du, Y. Bai, Z. Yang, R. Li, D. Zhang, Z. Ma, A. Yuan, J. Xu, Chin. Chem. Lett. **31**, 2309–2313 (2020)
32. J. Liu, Y. Zhou, Z. Xie, Y. Li, Y. Liu, J. Sun, Y. Ma, O. Terasaki, L. Chen, Angew. Chem. **59**, 1081–1086 (2020)
33. A. Zahoor, Z.K. Ghouri, S. Hashmi, F. Raza, S. Ishtiaque, S. Nadeem, I. Ullah, K.S. Nahm, ACS Sustain. Chem. Eng. **7**, 14288–14320 (2019)
34. C. Zhao, S. Liang, Y. Jiang, F. Gao, L. Xie, L. Chen, Mater. Lett. **270**, 127751 (2020)
35. Q. Sun, T. He, Y. Li, J. Mater. Chem. A **8**, 1687–1696 (2020)
36. J. Hu, L. Sun, F. Xie, Y. Qu, H. Tan, Y. Zhang, J. Mater. Chem. A **11**, 8380–8391 (2023)
37. P. Zhou, F. Xiao, R. Weng, Q. Huang, L. Wang, Q. He, W. Tang, P. Yang, R. Su, P. He, B. Jia, L. Bian, J. Mater. Chem. A **10**, 10514–10524 (2022)
38. K. Jayaramulu, M. Horn, A. Schneemann, H. Saini, A. Bakandritsos, V. Ranc, M. Petr, V. Stavila, C. Narayana, B. Scheibe, Š Kment, M. Otyepka, N. Motta, D. Dubal, R. Zbořil, R.A. Fischer, Adv. Mater. **33**, 2004560 (2021)
39. R. Abazari, S. Sanati, A. Morsali, D.P. Dubal, J. Mater. Chem. A **9**, 11001–11012 (2021)
40. P. Makkar, N.N. Ghosh, ACS Appl. Energy Mater. **3**, 2653–2664 (2020)
41. W. Guo, C. Dun, C. Yu, X. Song, F. Yang, W. Kuang, Y. Xie, S. Li, Z. Wang, J. Yu, G. Fu, J. Guo, M.A. Marcus, J.J. Urban, Q. Zhang, J. Qiu, Nat. Commun. **13**, 1409 (2022)
42. F.S. Farahani, M.S. Rahmanifar, A. Noori, M.F. El-Kady, N. Hassani, M. Neek-Amal, R.B. Kaner, M.F. Mousavi, J. Am. Chem. Soc. **144**, 3411–3428 (2022)